Check for updates

Robust method for uniform coating of carbon nanotubes with V_2O_5 for next-generation transparent electrodes and Li-ion batteries†

Daniil A. Ilatovskii, [a] Dmitry V. Krasnikov, [a] Anastasia E. Goldt, [a]
Seyedabolfazl Mousavihashemi, [b] Jani Sainio, [b] Eldar M. Khabushev, [a]
Alena A. Alekseeva, [a] Sergey Yu. Luchkin, [a] Zakhar S. Vinokurov, [c]
Alexander N. Shmakov, [c] Aly Elakshar, [a] Tanja Kallio [*b] and Albert G. Nasibulin [*a]

Composites comprising vanadium-pentoxide (V_2O_5) and single-walled carbon nanotubes (SWCNTs) are promising components for emerging applications in optoelectronics, solar cells, chemical and electrochemical sensors, *etc*. We propose a novel, simple, and facile approach for SWCNT covering with V_2O_5 by spin coating under ambient conditions. With the hydrolysis-polycondensation of the precursor (vanadyl triisopropoxide) directly on the surface of SWCNTs, the nm-thick layer of oxide is amorphous with a work function of 4.8 eV. The material recrystallizes after thermal treatment at 600 °C, achieving the work function of 5.8 eV. The key advantages of the method are that the obtained coating is uniform with a tunable thickness and does not require vacuuming or heating during processing. We demonstrate the groundbreaking results for two V_2O_5/SWCNT applications: transparent electrode and cathode for Li-ion batteries. As a transparent electrode, the composite shows stable sheet resistance of 160 Ω sq^{-1} at a 90% transmittance (550 nm) – the best performance reported for SWCNTs doped by metal oxides. As a cathode material, the obtained specific capacity (330 mA h g^{-1}) is the highest among all the other V_2O_5/SWCNT cathodes reported so far. This approach opens new horizons for the creation of the next generation of metal oxide composites for various applications, including optoelectronics and electrochemistry.

Introduction

Composite materials of carbon nanotubes and metal oxides are considered to be the key components of next-generation devices in electronics and energy applications.[1–5] For example, single-walled carbon nanotubes (SWCNTs) modified with vanadium pentoxide (V_2O_5) are promising to be applied in solar cells,[6–8] organic light-emitting diodes,[9–11] liquid crystal displays,[12,13] Li-ion batteries,[14,15] *etc*. Such a composite is also a great candidate for next-generation flexible and stretchable devices: supercapacitors,[16,17] skin-like passive electrodes,[18] and soft robotics.[19,20]

In particular, for transparent conductive films, V_2O_5 provides high optoelectronic performance acting as a p-type dopant of carbon nanotubes and contributes to chemical and mechanical stability with spectrally uniform optical transmittance.[21–24]

[a]Skolkovo Institute of Science and Technology, Bolshoy Boulevard 30, bd. 1, Moscow, 121205, Russian Federation. E-mail: A.Nasibulin@skol.tech
[b]Aalto University, Kemistintie 1, 02150 Espoo, Finland. E-mail: tanja.kallio@aalto.fi
[c]Boreskov Institute of Catalysis SB RAS, Lavrentieva Avenue 5, Novosibirsk, 630090, Russian Federation

† Electronic supplementary information (ESI) available. See DOI: https://doi.org/10.1039/d3ra04342h

Meanwhile, in electrodes for Li-ion batteries, V_2O_5 shows a high capacity and capability for reversible intercalation of Li-ions in the organic medium,[25] while SWCNTs serve as a suitable substrate with excellent electrical conductivity and large specific surface area. These applications demand uniform deposition of V_2O_5 on the SWCNT surface, which is usually achieved by thermal evaporation or solution-based coating, followed by heating.[26–29] However, both methods require additional energy input to provide thermal treatment, while aggregation of oxide particles[28] and even partial oxidation of SWCNTs might occur at an increased temperature.[30]

Hydrolysis-polycondensation reaction is a promising approach to the formation of metal oxides under ambient conditions and has several advantages: the process usually occurs at room temperature and atmospheric pressure allowing formation of a homogenous layer with tailored thickness and composition.[31–36] Though this method is highly suitable for the fine deposition of V_2O_5, it has never been employed for coating carbon nanotubes.

Here, we introduce the hydrolysis-polycondensation approach to deposit the V_2O_5 layer onto the SWCNT surface. With a set of methods (XPS, UV-vis-NIR spectroscopy, Raman spectroscopy, TEM, SEM, Kelvin Probe Force Microscopy, and *in situ* XRD), we examine the V_2O_5 formation and interaction with

carbon nanotubes and compare its properties with the common V_2O_5 layer deposited by thermal evaporation. We also assess the applicability of the obtained V_2O_5/SWCNT composites to construct transparent conductive films and electrodes for Li-ion batteries. The facile and potentially scalable approach for preparing V_2O_5/SWCNT composites exhibits great potential for application in optoelectronic, electrochemical, and other fields. Moreover, the approach proposed can be extended to obtain uniform coatings from other metal alkoxide precursors on the surface of various nanomaterials.

Experimental methods and materials

SWCNT synthesis

SWCNTs were synthesized by an aerosol (floating catalyst) chemical vapor deposition method using ferrocene as a catalyst precursor, toluene and C_2H_4 as hybrid carbon sources, and thiophene as a sulfur-based promoter.[37] The technique is described in detail elsewhere.[38,39] The synthesized SWCNTs were collected at the reactor outlet as a thin film of randomly oriented nanotubes on a nitrocellulose membrane filter (HAWP, Merck Millipore, USA). Then, the films were put by the dry transfer technique on quartz or Al substrates.[9] The size of the samples was 10×10 mm^2 with 90% transmittance at 550 nm for transparent electrodes and 17×17 mm^2 with 60% transmittance for the Li-ion battery electrodes.

V_2O_5 coating

V_2O_5 layer was formed on the surface of SWCNTs due to hydrolysis and polycondensation reactions in ambient conditions of vanadyl triisopropoxide (VTIP) (98%, Sigma-Aldrich) according to the scheme shown in Fig. 1. The precursor was diluted in isopropanol (99.5%, Sigma-Aldrich) with a volume ratio of 1 : 75, 1 : 100, 1 : 150, 1 : 200, 1 : 300, 1 : 400, 1 : 500, 1 : 600 and 1 : 1000 in a nitrogen atmosphere and then spin-coated (Ossila L2001A3-E461-EU) at the rate 4000 rpm for 60 s onto SWCNT film at ambient conditions.

Electrode preparation

Aluminum foils (20 μm thick, MTI Corporation) with diameters of 14 and 18 mm were cut using an electrode cutter (EL-Cut, EL-CELL) and wetted with pure ethanol (≥96.1 vol%, ETAX A). Free-standing SWCNT films (pristine reference and SWCNT coated with VTIP diluted in isopropanol with a volume ratio of 1 :

75) were transferred on top of the Al foil by pressing with polypropylene film, which acted as a separator. After removing pressure, the SWCNT films showed good adhesion to the Al surface due to ethanol wetting. The prepared electrodes were packed and dried under vacuum (∼0.05 mbar) at 80 °C for 12 hours to get rid of water and its effect on electrochemical experiments.

Electrochemical tests

The requirements for electrochemical measurements were taken from the protocol article.[40] The as-prepared electrodes were transferred into an Ar-filled glove box (Jacomex GP Campus) for coin cell (Hohsen 2016) and three-electrode cell assembling (EL-CELL®, ECC-Ref model). In a two-electrode cell, a Li foil was used as a counter electrode (Alfa Aesar, 0.75 mm thick); and glass fiber (Whatman GF/A, 19 mm in diameter, 0.26 mm thick) was used as a separator with 200 μl of a lithium hexafluorophosphate based electrolyte (BASF, LP30, 1 M LiPF$_6$ in 1 : 1 EC/DMC solution). Two parallel coin cells with good reproducibility were cycled by a LAND Battery Testing System (LAND CT2001®) at a constant temperature of 22 °C within the voltage range from 2.0 to 4.0 V. Various current densities were applied to evaluate the rate capability of the electrode materials. The charge and discharge current density for the rate capability tests varied from 0.1 to 10.0C (1C = 250 mA g^{-1}) in a constant current mode.[41] The C-rates were calculated based on the amount of the capacity obtained on the discharge step of the formation cycle.[42,43] In the first run, the cell was formatted with an estimated capacity based on the theoretical capacity, and then after the first formation cycle, experimental capacity was obtained. The capacity value from the formation cycle and mass of the electrode obtained from a 5-digit high precision scale was used to calculate the specific capacity. Cyclic voltammetry measurements were carried out in a three-electrode setup with a Bio-Logic potentiostat (MPG-205) by applying the potential of 2.0 to 4.0 V vs. Li$^+$/Li at 0.02 mV s^{-1} scan rate. A lithium wire was used as a reference electrode in the three-electrode setup while the other components were the same as for the coin cell setup. Another three-electrode cell was assembled to perform electrochemical impedance spectroscopy (EIS) before and after cycling. The EIS measurements were performed using an Autolab potentiostat (PGSTAT302 N, Nova 2.1 software). The alternating potential amplitude of 5 mV$_{rms}$ (root-mean-square) was applied to the cells in the frequency range of 1 MHz–15 mHz.
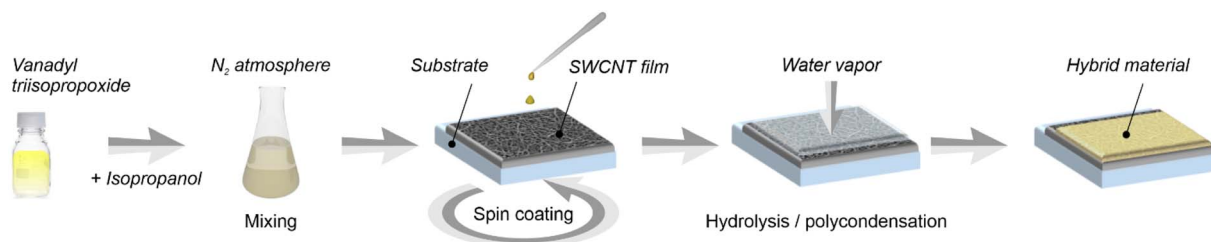

Fig. 1 Scheme of SWCNT coating at ambient conditions by nanometer-thick V_2O_5 layer using vanadyl triisopropoxide (VTIP) dissolved in isopropanol.

Characterization

UV-vis-NIR transmittance (T) spectra were measured using a PerkinElmer LAMBDA 1050 spectrophotometer. The sheet resistance of the samples was measured by a linear four-probe method using the Jandel RM3000 Test Unit. To compare the optoelectronic properties of the thin films, as a figure of merit we utilized an equivalent sheet resistance (R_{90}) – the sheet resistance of a film with a transmittance of $T = 90\%$ (at 550 nm) calculated according to the following equation:[44,45]

$$R_{90} = -\frac{\log(T/100\%) \cdot R_s}{\log(10/9)}, \tag{1}$$

where R_s is the sheet resistance of the examined film and $T\,(\%)$ is the transmittance at 550 nm.

The morphology of the films was investigated by transmission electron microscopy (TEM) using FEI Tecnai G2 F20. X-ray diffraction (XRD) data were collected using the Bruker D8 Advance diffractometer (CuKα). *In situ* synchrotron radiation XRD measurements were performed in the Siberian Synchrotron and Terahertz Radiation Centre at Budker Institute of Nuclear Physics. XRK-900 reactor chamber (Anton Paar, Austria) equipped with a fast, parallax-free one-coordinate X-ray detector OD-3M as well as a mass-spectrometer (UGA 100, Stanford Research Systems, USA) were used to heat V_2O_5/SWCNT. A standard sample (SRM676) was employed to calibrate the reflex positions at a wavelength of 0.1732 nm.

The climatic tests were carried out in the chamber KHTV-0.03 (Russia) in two regimes: in soft conditions at 25 °C and 40% relative humidity (RH) and in the regime of damp heat steady state at 35 °C and 100% RH and at 60 °C and 100% RH (standard: IEC 60068-2-78). The fitting of the data was carried out using OriginPro software applying the monomolecular growth model: $y = A(1 - e^{-k(x-xc)})$, where A – amplitude, xc – center, k – rate.[46]

Kelvin Probe Force Microscopy measurements were performed in a 2-pass amplitude modulation mode using a Pt-coated Si cantilever with a Cypher ES atomic force microscope (Asylum Research, Oxford Instruments) installed in an Ar-filled glove box (MBraun). The second pass height was 50 nm. The cantilever was calibrated on a ZYA-grade highly oriented pyrolytic graphite (HOPG).

Thermal evaporation of V_2O_5 powder (99.9%, Kurt J. Lesker Company) was carried out in a tungsten boat at 10^{-6} mbar (Pfeiffer turbo vacuum pump). The power of the source was increased slightly until an evaporation speed of 0.2 Å s^{-1} was stabilized. Further, the first 5 nm of the material was evaporated on a shutter, then the shutter was opened, and the evaporation proceeded with the rate maintained at the interval of 0.2–0.4 Å s^{-1} until the desired thickness of 30 nm was reached.

The reference composite for the optoelectronic performance test was produced by dispersing 1 g of V_2O_5 powder (99.9%, Kurt J. Lesker Company) in a mixture of isobutanol and benzyl alcohol in the ratio 180 : 12 ml with refluxing at 110 °C for 4 h,[47,48] followed by spin coating (Ossila L2001A3-E461-EU) on the surface of SWCNT film at the rate of 4000 rpm for 60 s at ambient conditions.

Elemental analysis was carried out by X-ray photoelectron spectroscopy (XPS) using a Kratos Axis Ultra spectrometer with monochromated Al Kα-radiation and charge neutralization, pass energy of 20 eV, X-ray power of 195 W and an analysis area of approximately 700 μm × 300 μm. The binding energy scale was referenced to the C 1s peak of SWCNTs at 284.4 eV. During the measurements, we observed a process of photoreduction of V^{5+} to V^{4+}, and therefore the measurement time was limited to a few minutes.[49] Peak fitting of the V 2p region was carried out using CasaXPS software after Shirley background subtraction. To fit properly the V 2p region, the background was extended over the O 1s peak which was also fitted (not shown). For each vanadium oxidation state Gaussian–Lorentzian peaks (GL(82) line shape in CasaXPS) with a V $2p_{1/2}$–V $2p_{3/2}$ splitting of 7.35 eV and a V $2p_{1/2}$/V $2p_{3/2}$ area ratio of 0.5 was used. Peak positions and full widths at half-maximum of the peaks were allowed to vary within reported limits.[50]

Results and discussion

V_2O_5/SWCNT composites

Hydrolysis-polycondensation of vanadyl triisopropoxide (VTIP) into a vanadium oxide affects the SWCNT properties complexly. According to UV-vis-NIR spectroscopy studies (Fig. 2a), transitions between van Hove singularities partially disappear (S_{11}, S_{22}, M_{11}) owing to charge transfer,[36,51] induced by p-type doping with V_2O_5. Notably, the absorbance of the SWCNT film does not significantly increase upon vanadium oxide deposition. The doping also manifests as a significant decrease in the film sheet resistance,[52] opening a route for application as an electrode in general and as a transparent electrode in particular. XPS measurements confirm the exclusive presence of vanadium pentoxide on the surface of the SWCNTs (Fig. 2b; the survey spectrum is shown in Fig. S1a†). We observe characteristic peaks of V^{5+} at 517.2 eV ($2p_{3/2}$) and 524.5 eV ($2p_{3/2}$). The peak corresponding to the trace amount of V^{4+} ($2p_{3/2}$ at 516.0 eV) is found to increase during the exposure and is most likely due to V^{5+} reduction by X-ray irradiation.[49] O 1s–V 2p region of bare V_2O_5 obtained by the scheme from Fig. 1 almost coincides with the same region for V_2O_5/SWCNT composite proving that interaction between carbon nanotubes and vanadium oxide is predominantly physical (Fig. S1b†).

TEM observation was carried out to investigate the morphology of the obtained V_2O_5/SWCNT composite, while pristine SWCNTs served as the reference (Fig. 2c). We observed homogeneous deposition of a thin film of vanadium oxide on the surface of SWCNTs (Fig. 2d) which can be accounted to efficient wetting of SWCNT surface with isopropanol (solvent for VTIP). The layer around SWCNTs can be *ca.* 1 nm and appears to be amorphous, which coincides with XRD measurements (Fig. S2a and b†) and selected area electron diffraction of the V_2O_5/SWCNT composites (the pattern does not contain rings corresponding to crystalline phases,[53] so we assume the structure to be amorphous). The thickness of the V_2O_5 layer can be varied by tuning the concentration of the VTIP solution. TEM morphology of the materials doped by 0, 9, and 42 μM solutions are shown in Fig. S2c–e.†
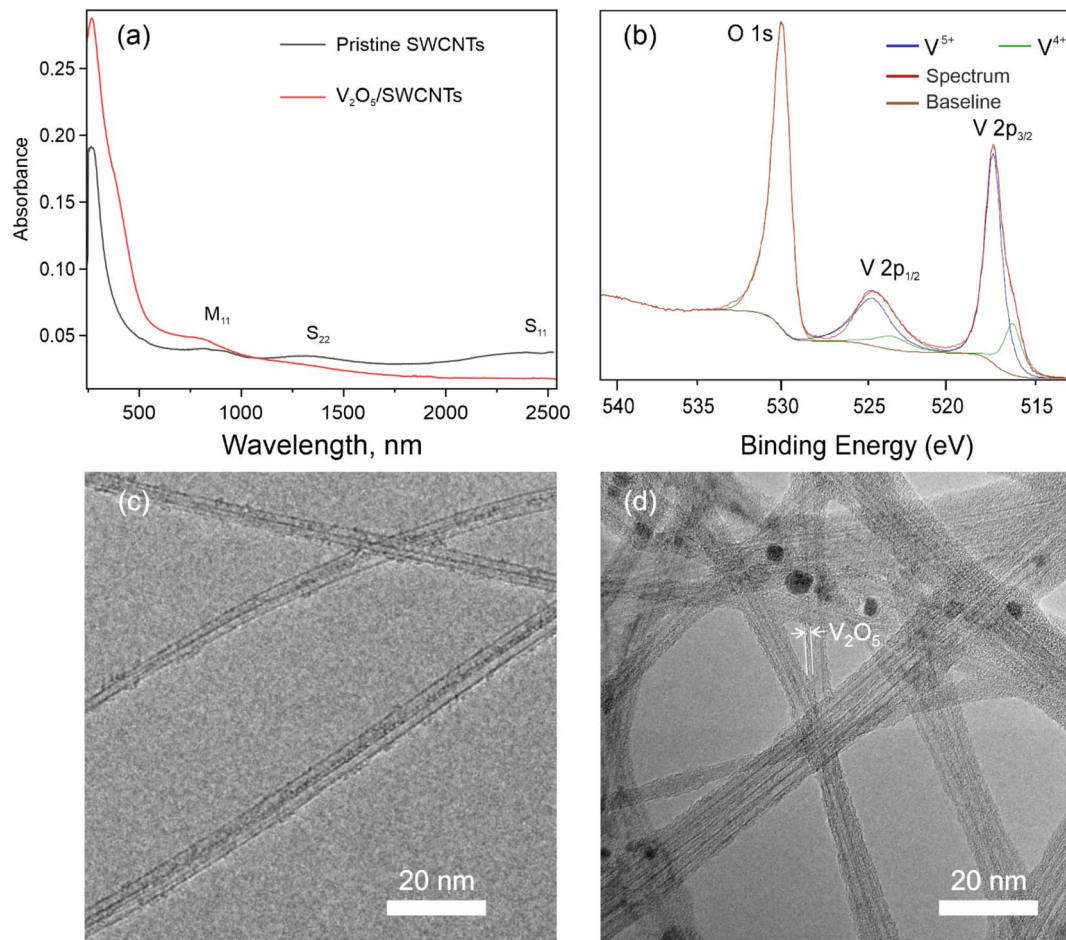
Fig. 2 . (a) UV-vis-NIR spectra of the pristine and V_2O_5-covered SWCNT films; (b) XPS spectrum (O 1s–V 2p region) of the V_2O_5/SWCNT composite material, (c) and (d) TEM images of pristine and V_2O_5-covered SWCNTs, respectively.

To highlight the hydrolysis-polycondensation mechanism peculiarities, we examined the influence of the process conditions, such as temperature and humidity. We employ a sheet resistance (R_s) of the composites as a facile non-invasive parameter to observe the evolution of materials and interaction between SWCNTs and V_2O_5. After the spin coating of VTIP/isopropanol upon the SWCNT films, we observe an immediate drop in the sheet resistance to a value, which we refer to as R_0. The raw data of R_s values are displayed in Table S2†.

We register a steady *ca.* 30% increase in the sheet resistance (Fig. 3a red curve) during the first month, while the following observation for around 2 months shows no further changes proving the doping stability in time. Interestingly, the evolution pattern shows no dependence on the vanadium oxide amount (Fig. 3a blue curve) or the presence of water or oxygen in storage (Fig. 3a violet curve). When the temperature was increased to 35 °C (Fig. 3b green curve) or 60 °C (Fig. 3b navy curve), we observed a similar 30% rise in the resistance values but within significantly shorter periods, *i.e.* 60 and 5 minutes, respectively; such a change in a rate for chemical process corresponds to the apparent activation energy *ca.* 190 kJ mol^{-1}.

When an SWCNT film was spin-coated by VTIP solution (9 μM) in a nitrogen glovebox (<0.1 ppm of water and oxygen), we

observed similar significant doping of SWCNTs reaching $R_{90} = 130$ Ω sq^{-1}, when compared to the equivalent sheet resistance of 330 Ω sq^{-1} of the undoped film. However, the evolution pattern for the sheet resistance under nitrogen is different (Fig. 3b orange curve) – the value of R_s steadily increases. This could be attributed to the evaporation of liquid VTIP without any V_2O_5 formation due to the lack of water-induced hydrolysis in the system.

Thus, we can address the mechanism of V_2O_5 formation from the VTIP solution. During spin coating (Fig. 1), isopropanol covers nanotubes and evaporates from the SWCNT surface; VTIP reacts with water vapor from the air to form the vanadium oxide coating. The hydrolysis-polycondensation mechanism is shown in Fig. 4.[35]

The simplified general reaction of complete hydrolysis of VTIP is:[54]

$$2VO(O–iPr)_3 + 3H_2O \rightarrow V_2O_5 + 6iPrOH. \quad (2)$$
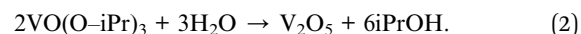
As it is found, VTIP/isopropanol solution enhanced the conductivity of the SWCNT films, which can be proven from the orange curve in Fig. 3b, when V_2O_5 is not formed. The rate of hydrolysis-polycondensation reaction strongly depends on
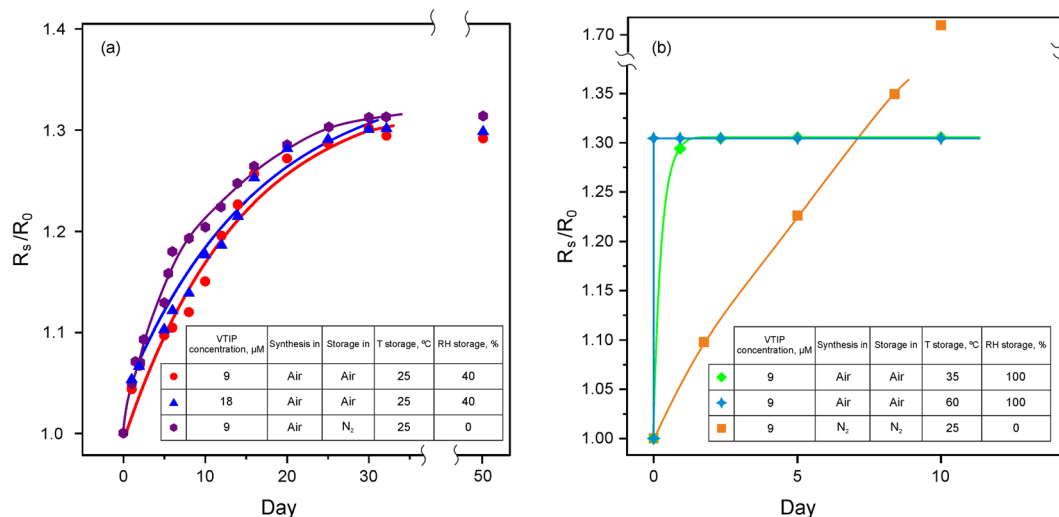
Fig. 3 Time evolution of normalized sheet resistance (R_0 is the initial sheet resistance) of the V_2O_5/SWCNT composite under different conditions: (a) at 25 °C and 40% RH, (b) increased temperature and RH, and the test of VTIP/V_2O_5 material.
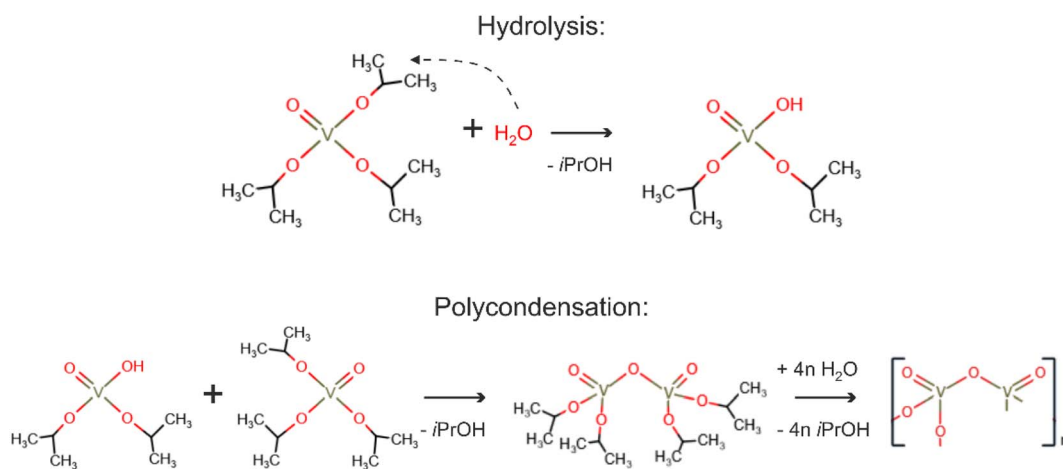

Fig. 4 2-step mechanism of hydrolysis–polycondensation of VTIP.

temperature; the activation energy is estimated to be *ca.* 190 kJ mol^{-1}, according to the temperature dependence of the sheet resistance shown in Fig. 3 at 25, 35, and 60 °C. This value most probably is attributed to the hydrolysis reaction (Fig. 4) as the slowest step of the process.[35] In the previous work,[55] the synthesis of V_2O_5 was characterized by activation energy twice lower, which may be explained by different precursors and the presence of a catalyst.

V_2O_5 is characterized by a high value of its work function up to 7.0 eV,[56] which is suitable for various applications: gas sensors, heterogeneous catalysts, organic photovoltaic devices, organic light-emitting diodes,[36,51,56] *etc.* When applied to an SWCNT film, a material with a high work function might effectively increase the conductivity due to doping.[37] Kelvin Probe Force Microscopy measurements were carried out to estimate the work function of the obtained materials (Fig. 5). Pristine V_2O_5 deposited from 9 μM VTIP solution possesses a relatively low work function of around 4.8 eV (Fig. 5a), so the V_2O_5 thin layer on a surface of SWCNTs

does not increase total work function of the composite (Fig. 5b) compared to the pristine SWCNTs (~4.8 eV) (Fig. S3†). As the reference, we measured the work function for the thermal-sputtered 30 nm V_2O_5 layer, which was also around 5 eV (Fig. 5c). Thus, thin amorphous layers of V_2O_5 obtained by hydrolysis-polycondensation and by thermal evaporation routes have rather low work functions, which might be increased to 5.8 eV by the sample annealing at 600 °C (Fig. 5d), when the crystalline phase appeared. However, the films became non-uniform, while extra defects could appear in the SWCNT structure due to the thermal treatment. These data coincide with *in situ* XRD studies: no additional reflexes appear after V_2O_5 deposition (Fig. S4†) while forthcoming heating in "air" shows recrystallization to the mixture of phases (most likely orthorhombic and monoclinic) appears after nanotube burning (Fig. S5†). Nevertheless, the V_2O_5 thin amorphous layer increases the conductivity of the SWCNT film, as it might cause charge exchange between SWCNTs and an absorbed oxide molecule leading to p-type
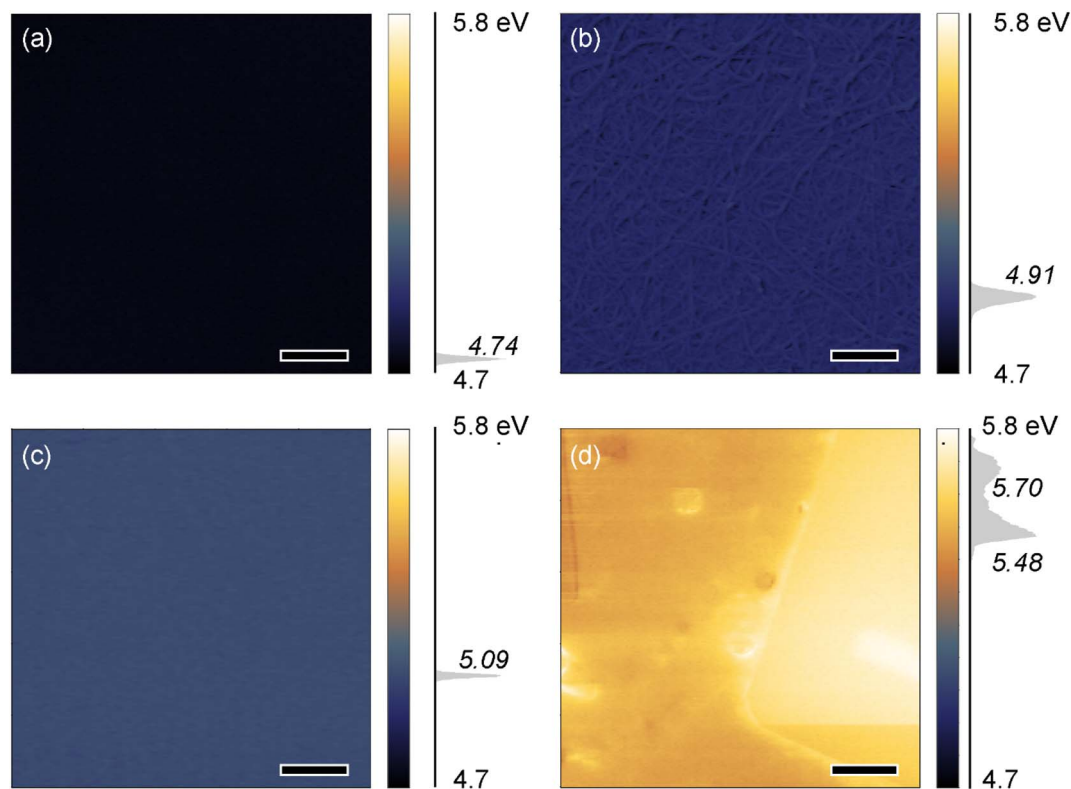
Fig. 5 Results of Kelvin probe force microscopy showing the work function map for (a) V_2O_5 deposited from VTIP solution, (b) the V_2O_5/SWCNT composite, (c) V_2O_5 deposited by thermal sputtering, (d) V_2O_5 deposited from VTIP solution and annealed at 600 °C in the air (scale bar is 1 μm).

doping.[36,51] It may also serve as a protective layer for SWCNTs preventing the influence of the environment on the characteristics of SWCNTs.

Overall, we propose the method for obtaining homogenous amorphous V_2O_5 coating on the surface of SWCNTs utilizing a hydrolysis-polycondensation route. The complete transformation to the V_2O_5 phase takes a few days at room temperature and could be significantly reduced in time to a couple of minutes at 60 °C. We investigated the change in the work function of the obtained composite and found practically no change when compared with the pristine SWCNTs. The work function of V_2O_5, however, could be increased by annealing at 600 °C.

Transparent conductive films based on V_2O_5/SWCNTs

High-quality pristine SWCNT films exhibit equivalent sheet resistance values above $R_{90} = 250$ Ω sq^{-1}.[44,45,58–61] The value of R_{90} can be significantly reduced by a certain post-synthesis procedure, among which adsorption doping is one of the most effective and robust.[17,22,62,63] The best conductivity improvement for carbon nanotubes was achieved by applying HNO_3,[9,60] $HAuCl_4$,[8,64] and $AuCl_3$ (ref. 44 and 65) as a dopant. Unfortunately, optoelectronic characteristics of the doped SWCNTs are always accompanied by poor time stability due to dopant desorption or decomposition.[66–69] To solve this problem, we could utilize stable inorganic compounds to simultaneously dope and protect SWCNTs.

As an example, Hellstrom *et al.* produced MoO_3/SWCNT structures by thermal evaporation of molybdenum oxide on

a substrate, followed by spray coating of carbon nanotubes. After the subsequent annealing, the films showed $R_{90} = 154$ Ω sq^{-1}. Over 20 days of monitoring, the equivalent sheet resistance of the films increased to $R_{90} = 170$ Ω sq^{-1}. Although the optoelectronic performance of the MoO_3/SWCNT structure is inferior to SWCNTs doped by HNO_3 or gold compounds, the stability of properties is noticeably higher. Despite the demonstrated perspective of the approach to use a transition metal oxide as a doping agent for SWCNTs, it has not been practically studied yet.

V_2O_5 is considered to be a promising dopant for SWCNTs as in the form of thin layers it possesses high transmittance and leads to p-type doping.[36,51] The increase in the VTIP concentration from 1 to 60 μM leads to a change in the equivalent sheet resistance of transparent conductive films that contain an extremum point (Fig. 6a): at the concentration of 9 μM the minimal $R_{90} = 130$ Ω sq^{-1} is achieved. The equivalent sheet resistance is the trade-off balance between the conductivity and transmittance of the sample (Fig. S6†). Up to the 9 μM concentration (Fig. S2e†), there is no significant change in the transmittance of the samples, while the resistance gradually decreases.

We suggest that at lower concentrations up to 9 μM the equivalent sheet resistance decreases noticeably because of the SWCNT coverage by the precursor. The consequent increase in the VTIP concentration does not contribute to the composite conductivity. However, it leads to a further decrease in the transmittance due to the formation of an extra V_2O_5 layer
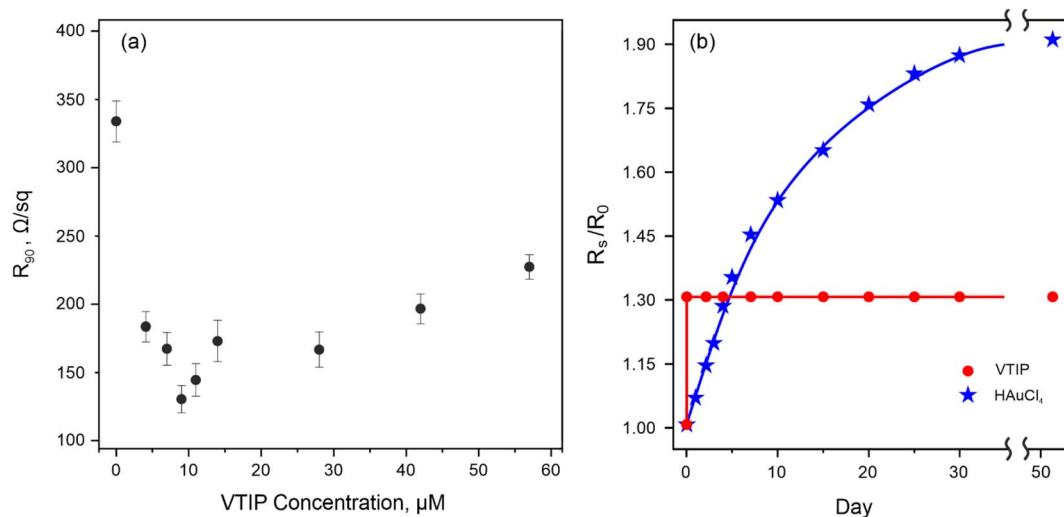
Fig. 6 V_2O_5/SWCNT composite as transparent conductive films: (a) concentration of dopant precursor *vs.* equivalent sheet resistance for an SWCNT/V_2O_5 transparent conductive film with the size of 1 cm^2; (b) stability of the conductivity for SWCNT-based for transparent conductive films covered by V_2O_5 and HAuCl$_4$.

(Fig. S2e†). We obtained the equivalent sheet resistance of $R_{90} = 130$ Ω sq^{-1}, which is among the lowest values for metal oxide doping.

We performed a stability test of SWCNTs doped by the highly effective dopant HAuCl$_4$ (ref. 8) to compare the doping stability with the V_2O_5 layer prepared by our method. For HAuCl$_4$-doped samples (30 μM solution in isopropanol), the resistance increased by 90% at 25 °C and 40% RH (Fig. 6b). For V_2O_5-doped samples pre-heated to 60 °C for 5 minutes (9 μM solution in isopropanol), the resistance increased only by 30% (the complete transformation discussed above) under the same conditions, proving that the composite is highly stable in its optoelectronic properties.

For a comparison of our method, we tested the performance of two extra V_2O_5/SWCNT composites. The first one was obtained by thermal evaporation of vanadium (V) oxide on the surface of a SWCNT film. The second one was fabricated by dispersing V_2O_5 powder in a mixture of benzyl- and isobutyl alcohols,[47,48] followed by spin coating of the dispersion on the SWCNT surface. The results of the optoelectronic performance of the composites are shown in Table 1.

The composite obtained by thermal evaporation possessed worse sheet resistance and transmittance compared to the hydrolysis-polycondensation sample. The higher value of R_s can be attributed to the less contact between the oxide and carbon nanotubes because thermal evaporation produces coating only

on a surface without penetration to deep layers of the SWCNT film, while transmittance decreases due to the higher thickness of the oxide coating. The sample produced from a dispersed V_2O_5 powder showed less efficiency of doping as well. R_s showed poor performance because the isobutanol/benzyl alcohol mixture may extend a reduction effect to the oxide making it a less effective dopant and giving a negative contribution to transmittance of the composite. Hence, the doping of SWCNTs by means of the hydrolysis-polycondensation method is preferable for the production of the highest optoelectronic performance.

To summarize this section, SWCNT film coating with VTIP solution at ambient conditions provides high stability doping for the SWCNTs. The 30% conductivity drop can be attributed to the completion of the hydrolysis-polycondensation reaction. The V_2O_5/SWCNT composite provides a stable value of the equivalent sheet resistance of $R_{90} = 160$ Ω sq^{-1}.

Cathode for Li-ion battery based on V_2O_5/SWCNTs

The specific capacity of V_2O_5 depends on the applied potential window determining the number of Li ions involved in electrochemical reactions during battery charging. The theoretical values for V_2O_5 are relatively high for a positive electrode material and equal to 294 and 440 mA h g^{-1} for 2 and 3 lithium ions, respectively. To investigate the applicability of the V_2O_5/

Table 1 Comparison of optoelectronic performance of V_2O_5/SWCNT composites under different synthesis methods

Route	T (550 nm), %	R_s, Ω sq^{-1}	R_{90}, Ω sq^{-1}
Thermal evaporation	89	180	199
Isobutanol/benzyl alcohol solution	88	190	231
Hydrolysis-polycondensation (this work)	90	160	160

SWCNT composite as a positive electrode in lithium batteries, three-electrode cells have been assembled and cycled between 2.0 to 4.0 V *vs.* Li$^+$/Li. In crystalline V$_2$O$_5$ compounds with well-defined crystal phases, sharp peaks in cyclic voltammograms are found due to fast phase changes during lithiation or delithiation.[70,71] Instead, voltammograms of amorphous V$_2$O$_5$ electrodes are featured with wide peaks for lithium reactions with vanadium oxide owing to the absence of clear phase transformations.[71]

Fig. S7† shows the cyclic voltammetry curves of the as-prepared SWCNT and V$_2$O$_5$/SWCNT electrode at a 0.02 mV s^{-1} scan rate. Observed wide peaks are characteristics of amorphous nano-V$_2$O$_5$ particles functioning as an active electrode material[71,72] meeting our observation of amorphous coating by TEM (Fig. S8†) and XRD (Fig. S2†).

The capacity of the V$_2$O$_5$/SWCNT electrode at the 0.02 mV s^{-1} scan rate is 330 mA h g^{-1}, which is higher than the corresponding values reported earlier for 3D V$_2$O$_5$/CNT cathodes.[70,73] To distinguish the capacity provided by V$_2$O$_5$ and the SWCNTs film, the electrochemical behavior of a reference sample with only the pristine SWCNT film has been examined in a similar cell setup. The electrode does not show any redox peaks in the cyclic voltammetry measurements. Yet, a huge amount of current is passed through the electrode at higher potentials, which indicates that SWCNTs react irreversibly with the electrolyte.[74]

The rate capability results of the V$_2$O$_5$/SWCNT electrodes are shown in Fig. 7. Increase of the current rate from 0.1 to 10C decreases capacity only from 280 to 210 mA h g^{-1}. This is due to the high electrical conductivity of SWCNTs and the nanostructured V$_2$O$_5$ layer, which shows very low polarization at the higher C rates indicating that this electrode has an excellent power performance. The rate capability measurements have

been performed only in a constant current mode, *i.e.* constant voltage has been not applied for the charge steps, which means that the reported discharge capacities are also affected by the polarization of the former charge step. It should be noted that the discharge-specific capacity values are higher in the case of constant current-constant voltage charge measurements. The energy efficiency remained around 90–95% for all the C rates up to 2C while increasing to 5 and 10C decreases the energy efficiency down to 87% and 83%, respectively. These results are in agreement with cyclic voltammetry results (Fig. S7†) since they show that the reaction of lithium with V$_2$O$_5$ (insertion) is more difficult than Li extraction from the structure. Capacity retention after the rate capability measurements is 99.89%, which shows the high stability of the electrode active material.

According to the long-term cycling results (Fig. S9†), the V$_2$O$_5$/SWCNT positive electrode provides 234 and 210 mA h g^{-1} in the first and 200th cycles, respectively, at the 1C rate. The minor scattering of the efficiency after the 30th cycle is observed, which corresponds to the capacity fading due to the side reaction between nanotubes and Li battery electrolyte causing changes in the functional groups of the nanotubes.[75–77] This interaction results in the partial release of V$_2$O$_5$ nanoparticles, followed by the capacity increase. The cell shows a high capacity retention of 96% after 100 cycles, which demonstrates good reversibility of the active composite material during charge and discharge cycling.

To investigate loss mechanism and electrode aging, impedance spectroscopy measurements were carried out. The resulting Nyquist plots of the V$_2$O$_5$/SWCNT electrode measured at the three-electrode system at the beginning of and after the above-mentioned long-term cycling together with the corresponding equivalent circuits are shown in Fig. S10.† The resistance is increased after 500 cycles as the electrode interface resistance
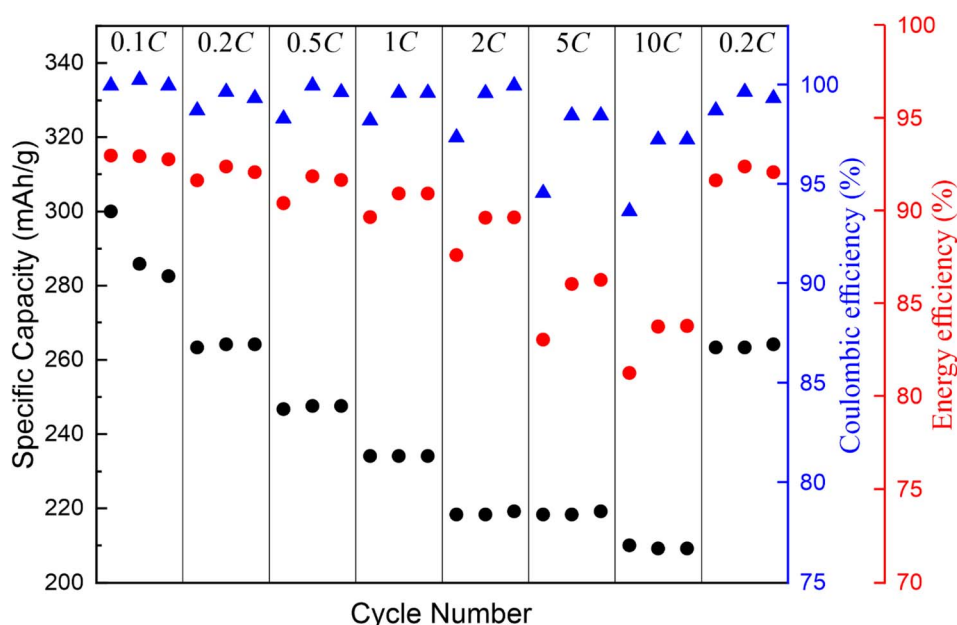

Fig. 7 Rate capability performance of V$_2$O$_5$/SWCNT in the coin cell assembly with the lithium counter electrode cycled between 2.0 to 4.0 V.

increases from 102 to 197 Ω and the charge transfer resistance increases from 613 to 898 Ω (Table S2†). The corresponding discussions are given in ESI.†

Overall, the V_2O_5/SWCNT composite as a cathode shows a high specific capacity of 330 mA h g^{-1}, which is the highest value among V_2O_5/SWCNT cathodes.[70,73] According to the transparency and low loading of oxide in composite, it may be applied, for instance, in microdevices working with low currents.[78,79]

Conclusions

In this work, we proposed a novel, simple, and fast method to cover SWCNTs with a uniform and continuous layer of V_2O_5 with tunable thicknesses. The method employs the synthesis based on the hydrolysis-polycondensation mechanism on the surface of SWCNTs, using vanadyl triisopropoxide as a precursor. We prove the coating to be amorphous vanadium pentoxide with a work function of 4.8 eV, which can be enhanced to 5.8 eV by high-temperature recrystallization at 600 °C. As a result, we fabricated the films with the equivalent sheet resistance of 160 Ω sq^{-1} (at $T = 90\%$), which is among the best for metal-oxide doping of carbon nanotubes. The material produced was also tested as a cathode for Li-ion batteries. It demonstrated the highest specific capacity of 330 mA h g^{-1} for V_2O_5/SWCNT cathodes. We expect our method to produce a thin layer of V_2O_5 coating around SWCNTs and other substrates to be useful in many applications, including electrochemistry, optoelectronics, and photovoltaics.

Author contributions

D. A. I., D. V. K., T. K., and A. G. N. made conceptualization of original ideas. D. A. I. made experiments in synthesis and transparent electrode construction. A. E. G. created a methodology for the quality estimation of transparent conductors. S. M. made experiments with Li-ion battery approbation. J. S. carried out XPS measurements. E. M. K. produced samples for XPS measurements. A. A. A. made XRD measurements. S. Yu. L. produced measurements of work function. Z. S. V. and A. N. S. obtained *in situ* XRD patterns. A. E. made thermal evaporation of V_2O_5. D. A. I. and S. M. wrote the original draft. D. V. K., T. K., and A. G. N. did supervision and reviewing/editing.

Conflicts of interest

There are no conflicts to declare.

Acknowledgements

References

1 L. Yu, C. Shearer and J. Shapter, *Chem. Rev.*, 2016, **116**, 13413–13453.

2 S. Mallakpour and E. Khadem, *Chem. Eng. J.*, 2016, **302**, 344–367.

3 T. A. Saleh, *Int. J. Sci. Res. Environ. Sci. Toxicol.*, 2017, **2**, 1–4.

4 P. Pathak, S. Park and H. J. Cho, *Micromachines*, 2020, **11**, 368.

5 F. Daneshvar, H. Chen, K. Noh and H. J. Sue, *Nanoscale Adv.*, 2021, **3**, 942–962.

6 A. E. Ostfeld, A. Catheline, K. Ligsay, K. C. Kim, Z. Chen, A. Facchetti, S. Fogden and A. C. Arias, *Appl. Phys. Lett.*, 2014, **105**(25), 253301.

7 T. A. Shastry and M. C. Hersam, *Adv. Energy Mater.*, 2017, **7**(10), 1601205.

8 P. M. Rajanna, H. Meddeb, O. Sergeev, A. P. Tsapenko, M. Vehse, O. Volobujeva, M. Danilson, P. D. Lund and G. Albert, *Nano Energy*, 2019, **67**, 104183.

9 A. Kaskela, A. G. Nasibulin, M. Y. Timmermans, B. Aitchison, A. Papadimitratos, Y. Tian, Z. Zhu, H. Jiang, D. P. Brown, A. Zakhidov and E. I. Kauppinen, *Nano Lett.*, 2010, **10**, 4349–4355.

10 A. I. Hofmann, W. T. T. Smaal, M. Mumtaz, D. Katsigiannopoulos, C. Brochon, F. Schütze, O. R. Hild, E. Cloutet and G. Hadziioannou, *Angew. Chem., Int. Ed.*, 2015, **54**, 8506–8510.

11 Z. R. Zhu, W. Geng, Q. Zhu, A. S. Ethiraj, T. Wang, L. C. Jing, Y. J. Ning, Y. Tian, W. H. Geng, L. Wu and H. Z. Geng, *Nanotechnology*, 2021, **32**(1), 015708.

12 N. Yamamoto, H. Makino, S. Osone, A. Ujihara, T. Ito, H. Hokari, T. Maruyama and T. Yamamoto, *Thin Solid Films*, 2012, **520**, 4131–4138.

13 Y. Park, I. Son, G. Moon, H. Cho, J. Lee and W. Jang, *Processes*, 2018, **6**, 108.

14 Y. Yue and H. Liang, *Adv. Energy Mater.*, 2017, **7**, 1–32.

15 F. Wang, D. Kozawa, Y. Miyauchi, K. Hiraoka, S. Mouri, Y. Ohno and K. Matsuda, *Nat. Commun.*, 2015, **6**, 1–7.

16 E. P. Gilshteyn, D. Amanbayev, A. S. Anisimov, T. Kallio and A. G. Nasibulin, *Sci. Rep.*, 2017, **7**(1), 17449.

17 M. Luo, Y. Liu, W. Huang, W. Qiao, Y. Zhou, Y. Ye and L. Sen Chen, *Micromachines*, 2017, **8**, 1–16.

18 E. P. Gilshteyn, S. Lin, V. A. Kondrashov, D. S. Kopylova, A. P. Tsapenko, A. S. Anisimov, A. J. Hart, X. Zhao and A. G. Nasibulin, *ACS Appl. Mater. Interfaces*, 2018, **10**, 28069–28075.

19 J. A. Rogers, T. Someya and Y. Huang, *Science*, 2010, **327**, 1603–1607.

20 S. A. Morin, R. F. Shepherd, S. W. Kwok, A. A. Stokes, A. Nemiroski and G. M. Whitesides, *Science*, 2012, **337**, 828–832.

21 X. Wang, Z. Liu and T. Zhang, *Small*, 2017, **13**, 1–19.

22 A. I. Hofmann, E. Cloutet and G. Hadziioannou, *Adv. Electron. Mater.*, 2018, **4**, 1700412.

23 J. Du, S. Pei, L. Ma and H. M. Cheng, *Adv. Mater.*, 2014, **26**, 1958–1991.

24 I. Jeon, K. Cui, T. Chiba, A. Anisimov, A. G. Nasibulin, E. I. Kauppinen, S. Maruyama and Y. Matsuo, *J. Am. Chem. Soc.*, 2015, **137**, 7982–7985.

25 V. Aravindan, Y. L. Cheah, W. F. Mak, G. Wee, B. V. R. Chowdari and S. Madhavi, *Chempluschem*, 2012, **77**, 570–575.

26 S. L. Hellstrom, M. Vosgueritchian, R. M. Stoltenberg, I. Irfan, M. Hammock, Y. B. Wang, C. Jia, X. Guo, Y. Gao and Z. Bao, *Nano Lett.*, 2012, **12**, 3574–3580.

27 R. Senthilkumar, G. Anandhababu, T. Mahalingam and G. Ravi, *J. Energy Chem.*, 2016, **25**, 798–804.

28 D. Vasanth Raj, N. Ponpandian, D. Mangalaraj and C. Viswanathan, *Mater. Sci. Semicond. Process.*, 2013, **16**, 256–262.

29 C. Ban, N. A. Chernova and M. S. Whittingham, *Electrochem. Commun.*, 2009, **11**, 522–525.

30 E. Mansfield, A. Kar and S. A. Hooker, *Anal. Bioanal. Chem.*, 2010, **396**, 1071–1077.

31 A. V. Vinogradov and V. V. Vinogradov, *RSC Adv.*, 2014, **4**, 45903–45919.

32 V. V. Vinogradov, A. V. Agafonov, A. V. Vinogradov, T. I. Gulyaeva, V. A. Drozdov and V. A. Likholobov, *J. Sol-Gel Sci. Technol.*, 2010, **56**, 333–339.

33 D. A. Ilatovskii, A. V Vinogradov, V. Milichko, V. V Vinogradov and R. Soc, *Open Sci.*, 2018, **5**, 172465.

34 D. Avnir, S. Braun, O. Lev and M. Ottolenghi, *Chem. Mater.*, 1994, 1605–1614.

35 N. Özer, *Thin Solid Films*, 1997, **305**, 80–87.

36 J. Meyer, S. Hamwi, M. Kröger, W. Kowalsky, T. Riedl and A. Kahn, *Adv. Mater.*, 2012, **24**, 5408–5427.

37 A. R. Bogdanova, D. V. Krasnikov and A. G. Nasibulin, *Carbon*, 2023, **210**, 118051.

38 O. Reynaud, A. G. Nasibulin, A. S. Anisimov, I. V. Anoshkin, H. Jiang and E. I. Kauppinen, *Chem. Eng. J.*, 2014, **255**, 134–140.

39 E. M. Khabushev, D. V. Krasnikov, A. E. Goldt, E. O. Fedorovskaya, A. P. Tsapenko, Q. Zhang, E. I. Kauppinen, T. Kallio and A. G. Nasibulin, *Carbon*, 2022, **189**, 474–483.

40 J. Li, C. Arbizzani, S. Kjelstrup, J. Xiao, Y. Xia, Y. Yu, Y. Yang, I. Belharouak, T. Zawodzinski, S.-T. Myung, R. Raccichini and S. Passerini, *J. Power Sources*, 2020, **452**, 227824.

41 Z. Chen, D. Steinle, H. D. Nguyen, J. K. Kim, A. Mayer, J. Shi, E. Paillard, C. Iojoiu, S. Passerini and D. Bresser, *Nano Energy*, 2020, **77**, 105129.

42 M. X. Tran, P. Smyrek, J. Park, W. Pfleging and J. K. Lee, *Nanomaterials*, 2022, **12**, 1–10.

43 H. Gao, X. Zeng, Y. Hu, V. Tileli, L. Li, Y. Ren, X. Meng, F. Maglia, P. Lamp, S. J. Kim, K. Amine and Z. Chen, *ACS Appl. Energy Mater.*, 2018, **1**, 2254–2260.

44 I. V. Anoshkin, A. G. Nasibulin, Y. Tian, B. Liu, H. Jiang and E. I. Kauppinen, *Carbon*, 2014, **78**, 130–136.

45 D. A. Ilatovskii, E. P. Gilshtein, O. E. Glukhova and A. G. Nasibulin, *Adv. Sci.*, 2022, **2201673**, 1–16.

46 OriginLab Corporation Official Website, https://www.originlab.com/doc/Origin-Help/MnMolecular-FitFunc, (accessed 20 July 2023).

47 X. Wei, S. Li, W. Li, X. Dong, J. Gou, Z. Chen, Z. Wu, T. Wang and Y. Jiang, *Integr. Ferroelectr.*, 2014, **153**, 126–132.

48 J. Livage, *Solid State Ionics*, 1996, **86–88**, 935–942.

49 S. P. Chenakin, R. P. Silvy and N. Kruse, *J. Phys. Chem. B*, 2005, **109**, 14611–14618.

50 M. C. Biesinger, L. W. M. Lau, A. R. Gerson and R. S. C. Smart, *Appl. Surf. Sci.*, 2010, **257**, 887–898.

51 M. T. Greiner, L. Chai, M. G. Helander, W. M. Tang and Z. H. Lu, *Adv. Funct. Mater.*, 2012, **22**, 4557–4568.

52 M. V. Kharlamova, *Prog. Mater. Sci.*, 2016, **77**, 125–211.

53 B. D. Gauntt, E. C. Dickey and M. W. Horn, *J. Mater. Res.*, 2009, **24**, 1590–1599.

54 J. Livage, *Chem. Mater.*, 1991, **3**, 578–593.

55 J.-P. W. Q. Wen, J.-F. Huang and L.-Y. Cao, *J. Synth. Cryst.*, 2011, **40**, 1242–1245.

56 A. D'elia, C. Cepek, M. De Simone, S. Macis, B. Belec, M. Fanetti, P. Piseri, A. Marcelli and M. Coreno, *Phys. Chem. Chem. Phys.*, 2020, **22**, 6282–6290.

57 A. P. Tsapenko, S. A. Romanov, D. A. Satco, D. V. Krasnikov, P. M. Rajanna, M. Danilson, O. Volobujeva, A. S. Anisimov, A. E. Goldt and A. G. Nasibulin, *J. Phys. Chem. Lett.*, 2019, **10**, 3961–3965.

58 Y. Zhou, L. Hu and G. Grüner, *Appl. Phys. Lett.*, 2006, **88**, 14–17.

59 K. Mustonen, P. Laiho, A. Kaskela, T. Susi, A. G. Nasibulin and E. I. Kauppinen, *Appl. Phys. Lett.*, 2015, **107**, 1–6.

60 A. Hussain, Y. Liao, Q. Zhang, E. X. Ding, P. Laiho, S. Ahmad, N. Wei, Y. Tian, H. Jiang and E. I. Kauppinen, *Nanoscale*, 2018, **10**, 9752–9759.

61 E. M. Khabushev, D. V. Krasnikov, O. T. Zaremba, A. P. Tsapenko, A. E. Goldt and A. G. Nasibulin, *J. Phys. Chem. Lett.*, 2019, **10**, 6962–6966.

62 S. Jiang, P. X. Hou, C. Liu and H. M. Cheng, *J. Mater. Sci. Technol.*, 2019, **35**, 2447–2462.

63 Q. Zhang, N. Wei, P. Laiho and E. I. Kauppinen, *Top. Curr. Chem.*, 2017, **375**, 1–30.

64 A. P. Tsapenko, A. E. Goldt, E. Shulga, Z. I. Popov, K. I. Maslakov, A. S. Anisimov, P. B. Sorokin and A. G. Nasibulin, *Carbon*, 2018, **130**, 448–457.

65 K. K. Kim, S. M. Yoon, H. K. Park, H. J. Shin, S. M. Kim, J. J. Bae, Y. Cui, J. M. Kim, J. Y. Choi and Y. H. Lee, *New J. Chem.*, 2010, **34**, 2183–2188.

66 L. Yu, T. Grace, M. Batmunkh, M. Dadkhah, C. Shearer and J. Shapter, *J. Mater. Chem. A*, 2017, **5**, 24247–24256.

67 I. W. Peter Chen, R. Liang, H. Zhao, B. Wang and C. Zhang, *Nanotechnology*, 2011, **22**, 485708.

68 L. D'Arsié, S. Esconjauregui, R. S. Weatherup, X. Wu, W. E. Arter, H. Sugime, C. Cepek and J. Robertson, *RSC Adv.*, 2016, **6**, 113185–113192.

69 D. S. Kopylova, D. A. Satco, E. M. Khabushev, A. V. Bubis, D. V. Krasnikov, T. Kallio and A. G. Nasibulin, *Carbon*, 2020, **167**, 244–248.

70 X. Yao, G. Guo, P.-Z. Li, Z.-Z. Luo, Q. Yan and Y. Zhao, *ACS Appl. Mater. Interfaces*, 2017, **9**, 42438–42443.

71 F. Mattelaer, K. Geryl, G. Rampelberg, J. Dendooven and C. Detavernier, *ACS Appl. Mater. Interfaces*, 2017, **9**, 13121–13131.

72 A. Pan, J. G. Zhang, Z. Nie, G. Cao, B. W. Arey, G. Li, S. Q. Liang and J. Liu, *J. Mater. Chem.*, 2010, **20**, 9193–9199.

73 Q. Li, Y. Chen, J. He, F. Fu, F. Qi, J. Lin and W. Zhang, *Energy Technol.*, 2017, **5**, 665–669.

74 B. J. Landi, M. J. Ganter, C. D. Cress, R. A. DiLeo and R. P. Raffaelle, *Energy Environ. Sci.*, 2009, **2**, 638–654.

75 K. Hasegawa and S. Noda, *J. Power Sources*, 2016, **321**, 155–162.

76 J. Landesfeind and H. A. Gasteiger, *J. Electrochem. Soc.*, 2019, **166**, A3079–A3097.

77 S. Mousavihashemi, K. Lahtinen and T. Kallio, *Electrochim. Acta*, 2022, **412**, 140093.

78 N. J. Dudney, *Electrochem. Soc. Interface*, 2008, **17**, 44–48.

79 S. Ferrari, M. Loveridge, S. D. Beattie, M. Jahn, R. J. Dashwood and R. Bhagat, *J. Power Sources*, 2015, **286**, 25–46.